metals

MDPI

Article

Mechanical Behavior of Fe- and Co-Based Amorphous Alloys after Thermal Action

Inga Permyakova [1,*] and Alex Glezer [1,2]

[1] Scientific Center of Metal Science and Metal Physics, Bardin Central Research Institute of Ferrous Metallurgy, Radio St. 23/9, bld. 2, 105005 Moscow, Russia; a.glezer@mail.ru
[2] Department of Physical Materials, National University of Science and Technology "MISIS", Leninskii Pr. 4, 119049 Moscow, Russia
* Correspondence: inga_perm@mail.ru; Tel.: +7-495-777-93-50

Abstract: The effect of heat treatment on the structure and mechanical properties of Co-Fe-Cr-Si-B/Fe-Cr-B/Fe-Ni-B amorphous alloys has been studied systematically. Melt-quenching (spinning method) was used for production of investigated amorphous alloys. The transmission electron microscopy (TEM) was used to study the structure transformations. The effect of temperature on deformation behavior (plasticity, microhardness, crack resistance, and the density and average length of shear bands) of the amorphous alloys was studied by bending and microindentation. It is shown that the ductile–brittle transition, which occurs at the stage of structure relaxation in amorphous alloys, is caused by two factors: a decrease in the susceptibility of the amorphous matrix to plastic flow and an abrupt decrease in the resistance to the development of quasibrittle cracks. It is established that the transition to a two-phase amorphous–nanocrystalline state upon annealing leads to substantial strengthening of the alloys and a partial recovery of their plasticity. It is proved that the strengthening of amorphous alloys at the initial stages of crystallization can be initiated by the difference in the elastic moduli of the amorphous matrix and the precipitated nanocrystals, as well as by the specific features of the interaction between nanocrystalline phase particles and shear bands propagating under external actions. It is established that the phenomenon of plasticization in amorphous alloys (the crack resistance can increase after annealing in a certain temperature range) is due to the effective retardation of cracks on nanoparticles.

Keywords: amorphous alloy; structure; hardness; plasticity; shear band; crack resistance; ductile–brittle transition; nanocrystal; TEM; indentation

check for updates

Citation: Permyakova, I.; Glezer, A. Mechanical Behavior of Fe- and Co-Based Amorphous Alloys after Thermal Action. *Metals* **2022**, *12*, 297. https://doi.org/10.3390/met12020297

Academic Editors: Vitaly A. Khonik and Jordi Sort

Received: 17 January 2022
Accepted: 7 February 2022
Published: 9 February 2022

Publisher's Note: MDPI stays neutral with regard to jurisdictional claims in published maps and institutional affiliations.

Copyright: © 2022 by the authors. Licensee MDPI, Basel, Switzerland. This article is an open access article distributed under the terms and conditions of the Creative Commons Attribution (CC BY) license (https://creativecommons.org/licenses/by/4.0/).

1. Introduction

Amorphous alloys (AAs) exhibit unique and practically important properties due to an unusual structural state with a predominance of short-range order in the arrangement of atoms and the absence of translation symmetry over long distances [1–3]. One of the main problems preventing the widespread use of such materials is the limited range of their thermal stability [4,5]. Under external actions (in particular, upon heating), the degree of structure disorder of AAs decreases. The rearrangements are possible both in the amorphous state at the stage of structure relaxation and upon the precipitation of nanocrystalline phases at the stage of crystallization [6–9]. In turn, this leads to significant changes in the properties of AAs. At present, there remain topical and controversial issues related to the ductile–brittle transition of AAs and their deformation behavior upon the transition from the amorphous to the nanocrystalline state [9–13]. Plastic deformation in AAs occurs mostly according to the dislocation-free mechanism due to the formation and development of strongly localized shear bands in the absence of strengthening effects [14]. It ensures the catastrophic nature of the destruction [3,15]. The strength and plasticity of these alloys can be increased by transforming an amorphous structure into a quasiamorphous one or into a partially nanocrystalline one, for example, during the heat treatment of

AAs [1,16,17]. The uniqueness of amorphous–nanocrystalline structures resides in the fact that the phase components of the system are radically different in the nature of their atomic structure: on the one side, there is a crystalline constituent with a regular arrangement of atoms, in accordance with the laws of translational symmetry, and on the other side, an amorphous constituent with a disordered, statistical arrangement of atoms in space. This "symbiosis" leads to a number of effects that influence the mechanical behavior of these materials [9,11,12,18]. The situation is aggravated if the crystalline phase in the amorphous–crystalline state has nanocrystalline scales (less than 100 nm). The transition process from amorphous to the crystalline state during annealing in the given temperature–time intervals will be carried out by the formation of nanocrystals in the amorphous matrix. Thus, natural amorphous–nanocrystalline composites with the best combination of properties are formed [19–21]. Two limiting cases of formation of amorphous–nanocrystalline structure can be conditionally distinguished during crystallization of amorphous alloys: Type I, in which nanocrystals (their volume fraction V_v does not exceed $\approx$ 0.3–0.4) are uniformly distributed in an amorphous matrix and do not contact each other, and Type II, in which nanocrystals fill the entire volume almost completely and are separated by thin amorphous intercrystalline interlayers. A wide variety of amorphous–nanocrystalline structures can be formed between these limiting structural states. Their mechanical behavior has not been well studied. Mechanisms of plastic deformation and fracture of a wide range of amorphous and amorphous–nanocrystalline materials and regularities the formation of their properties continue to be urgent issues. The aim of this work was a comprehensive study of the changes in the mechanical properties (plasticity, hardness, crack resistance) of the cobalt- and iron-based AAs in combination with their structure transformations occurring in a wide range of annealing temperatures.

Seven compositions of amorphous alloys from the "metal–metalloid" group were studied. The glass transition temperature of these alloys is below the crystallization temperature. In almost all cases, the structures and properties were studied on the same samples. The choice of such a wide group of alloys was due to a number of reasons:

- We selected simple "model" systems (Fe-Ni-B type) to study the general patterns of crystallization when two or three phases are formed (which simplifies the interpretation of the results obtained), and we selected complex multicomponent systems, during crystallization of which more complex structures are formed. The main metallic components of AA were iron, cobalt, nickel; as additional components (metals and metalloids), elements were used that differ in solubility in the crystal lattice of the main metal component of the alloy.
- The compositions of the studied alloys were selected in such a way that they could be expected to exhibit different crystallization mechanisms: primary, eutectic.
- There was a need to understand whether the observed phenomena are typical or characteristic of only one particular system.

The Co-Fe-Cr-Si-B AA is related to corrosion-resistant materials due to the presence of chromium in the composition. These alloys exhibit resistance to impacts and vibrations, high electrical resistivity, low coercive force, and low magnetization-reversal loss over a wide frequency range. The high-cobalt amorphous alloys are characterized by near-zero saturation magnetostriction and very high magnetic permeability. For this reason, such AAs show promise as materials for magnetic shields. In addition, high-permeability iron–cobalt AAs can replace permalloys with high induction in radio-electronic equipment. Co-Fe-Cr-Si-B AAs surpass permalloys in some properties and manufacturability. Ribbons of cobalt-based AAs are used in the cores of small-sized high-frequency transformers for various purposes. They are used in current leakage detectors, for magnetic read/write heads, as temperature-sensitive sensors, and as highly sensitive modulating magnetic converters.

Amorphous alloys of Fe–*T*–B (*T* is an atom of a transition element, such as Cr or Ni) are the basis of magnetically soft and magnetically hard materials and protective coatings, some compositions of which are widely used for radio engineering and electronics. The use

of AA ribbons with a high Fe content in power transformers is promising. However, this requires a change in the technology of their manufacture: winding the tape on the coils of transformers, annealing in a magnetic field and in an inert environment, and special conditions for sealing and impregnating the cores. Iron–nickel alloys are characterized by high magnetic permeability, low coercive force, and high squareness of the hysteresis loop. They are comparable to metal magnetic alloys and ferrites in saturation induction. All this makes it possible to use them for the manufacture of transformers and electromagnetic devices operating at elevated frequencies potentially.

Ternary AAs of the Fe-Ni-B ($Fe_{58}Ni_{25}B_{17}$, $Fe_{53.3}Ni_{26.5}B_{20.2}$, $Fe_{50}Ni_{33}B_{17}$) system are model alloys. External actions on the Fe-Ni-B AAs cause precipitation of a Fe-Ni nanocrystalline phase which can vary in crystal lattice types (BCC, FCC) depending on the ratio between the iron and nickel concentrations. Thus, it is possible to establish the effect of the type crystal lattice of nanocrystals on the mechanical behavior of materials with an amorphous–nanocrystalline structure. In addition, partial crystallization can favor changes in their soft magnetic characteristics.

2. Materials and Methods

The investigated alloys were prepared by melt quenching. In the melt-spinning process, a certain amount (50 g) of small pieces of an alloy is placed inside a crucible (made of quartz glass) surrounded by an induction coil. Applying a high current leads to an increase in the temperature of the alloy inside the crucible; accordingly, it melts. Then the molten metallic jet is ejected by Ar pressurization through a fine nozzle onto a fast-rotating copper wheel, which rotates at 2500–6000 rpm. Such a high rotation rate offers the rapid solidification rates (10^5–10^6 K/s) that are required to freeze the atoms of the liquid phase (molten metal) into solid amorphous solid. The geometric parameters of the melt-spun iron- and cobalt-based AA ribbons under study as well as the ranges of their isothermal annealing conditions used for the formation of amorphous–nanocrystalline structure are given in Table 1.

Table 1. Geometrical parameters of AA ribbons and temperature–time ranges of their heat treatment.

Composition, at.%	Thickness h, μm	Width b, mm	Temperature T_{an}, K	Holding Time t, min–h
$Co_{70.5}Fe_{0.5}Cr_4Si_7B_{18}$	30	20	323–898	10–30 min
$Co_{28.2}Fe_{38.9}Cr_{15.4}Si_{0.3}B_{17.2}$	25	10	373–973	10–30 min
$Fe_{60.8}Co_{20.2}B_{14}Si_5$	20	10	323–923	10–30 min
$Fe_{53.3}Ni_{26.5}B_{20.2}$	25	10	373–798	10–30 min
$Fe_{50}Ni_{33}B_{17}$	20	10	523–723	30 min–2 h
$Fe_{58}Ni_{25}B_{17}$	20	10	523–723	30 min–2 h
$Fe_{70}Cr_{15}B_{15}$	35	5	713–793	30 min–2 h

The amorphous and crystalline phases in the alloys were identified by transmission electron microscopy (TEM) with a JEM 1400 microscope (Jeol Ltd., Tokyo, Japan) at an accelerating voltage of 120 kV.

The plasticity of the AAs was assessed by the *U*-method (by bending deformation) according to the following formula:

$$\varepsilon = h/(d - h), \quad (1)$$

where h is the thickness of AA, d is the distance between the plane-parallel plates, to which the ends of the AA ribbon came close at the moment of failure by arcuate bending [22–25].

The microhardness of the AA samples was measured by indentation with a Vickers pyramid using an MHT-3M microhardness tester (Lomo, St. Petersburg, Russia) at a load of 0.40 N by a standard technique.

The traditional methods for assessment of crack resistance (fracture toughness) K_{1c}—three- and four-point notched specimen bending, eccentric tension, double torsion, and

others [26]—require labor-intensive stages of mechanical machining, special testing equipment, and a significant number of specimens of complex shape (with cut layers, holes, notches). Conventional methods for measuring crack resistance are not suitable for samples of small dimensions and thin thickness, such as thin ribbons of amorphous alloys. Therefore, microindentation in this sense is a promising method of mechanical testing [25–28] that makes it possible to evaluate important mechanical characteristics simply, quickly, and without macrofailures. Fracture toughness K_{1c} was calculated by the following formula:

$$K_{1c} = A(E/HV)^{1/2}P/C^{3/2}, \quad (2)$$

where A = 0.016 is the calibration coefficient of proportionality for thin ribbons of amorphous alloys, E is the Young's modulus measured by dynamic indentation methods, HV is the Vickers microhardness, P is the critical load for the appearance of radial cracks upon local loading of the AA samples, and C is the average crack length [25,27,29]. The indentation of amorphous alloys was carried out only on the sample plane.

The measurement error of microhardness is no more than 4%; crack resistance, ≤15%; and plasticity, ≤12%. The error in estimating the structural parameters (i.e., size and volume fraction of nanocrystals) is no more than 10%.

3. Results and Discussion

3.1. The Phenomenon of AA Embrittlement

The phenomenon of embrittlement, i.e., the loss of the ability of plastic deformation at the macroscopic level after annealing within the limits of the existence of the amorphous state, is well known for the AAs of metal–metalloid type [10,30–32]. According to Kimura and Masumoto [33], an abrupt decrease in crack resistance is caused by structure rearrangements in the amorphous matrix. They lead to an intense drop in the so-called "microfracture stress", in other words, to an abrupt decrease in the external stress, at which point quasibrittle cracks begin to spontaneously develop. Moreover, according to [33], the tendency to form shear bands, i.e., the tendency to exhibit plastic flow, does not decrease in the amorphous matrix.

The loss of plasticity ε_f of the Fe-Ni-B AA occurs in one step, in contrast to that in the Co-Fe-Cr-Si-B AA (Figure 1), in which two stages are observed with a slight increase in the ε_f parameter in the precrystallization temperature range between 673 and 723 K.

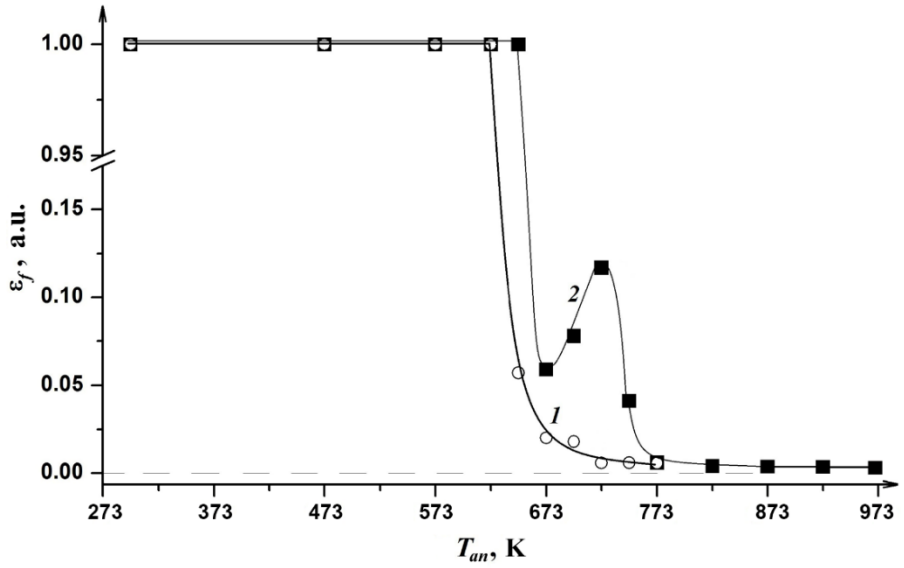


Figure 1. Effect of heat treatment on the plasticity ε_f of AAs: *1*, $Fe_{53.3}Ni_{26.5}B_{20.2}$; *2*, $Co_{28.2}Fe_{38.9}Cr_{15.4}Si_{0.3}B_{17.2}$.

The difference between the alloys with respect to their ε_f dependences is associated with different quenching rates upon their preparation: a higher rate of 2.6×10^6 K/c (for the $Fe_{53.3}Ni_{26.5}B_{20.2}$ alloy) leads to a one-stage decrease in plasticity, while a lower rate of 1.0×10^6 K/c (for the $Co_{28.2}Fe_{38.9}Cr_{15.4}Si_{0.3}B_{17.2}$ alloy) leads to two stages of decrease in ε_f. It is important to keep in mind that loss of plasticity and ductile–brittle transition temperature in AAs depend on alloy composition, quenching rate, and annealing conditions [34–37]. In turn, the quenching rate is also related to the maximum thickness of the amorphous alloy formed during production on special equipment for melt quenching. This makes it possible to evaluate the ability of alloys to undergo amorphization [38].

The nature of AA embrittlement is rather complex and is associated with a number of factors. First, nonmetal atoms make a substantial contribution to the embrittlement process. Such atoms due to their ability to quickly diffuse upon annealing can form aggregates, which cause local stresses at the boundary with the amorphous matrix. This stimulates a decrease in the plasticity of segregation areas. Second, the elements that make up the basis of AAs are also important. It is known that crystalline transition metals with a BCC lattice are more susceptible to embrittlement than metals with an FCC lattice. In the AA, the coordination number is $Z \approx 12$, which corresponds to FCC/HCP structures. Upon aging caused by annealing, a short-range order changes, and, accordingly, Z of the AA changes to Z of the crystalline element (in our case, $Z = 8$ for one of the first precipitated BCC α-Fe phases in both alloys). Thus, the internal stresses promoting the ductile–brittle transition can arise in the AA upon heat treatment in the course of establishing the order characteristic of the BCC lattice.

In addition, there is experimental evidence that the magnetization direction varies from transverse to longitudinal in annealed (brittle) AA ribbons [39–41]. An increase in tensile stress can be associated with positive magnetostriction in volume. In this regard, the embrittlement of the Fe-Ni-B AA can be explained by the assumption of the presence of BCC-type regions with local short-range order included in the amorphous Fe-Ni-based matrix with an Invar effect. The thermal expansion of the matrix is small, while the thermal expansion of the ordered areas is similar to that of BCC Fe. Such a difference in thermal expansion can cause thermal stresses in the AA upon cooling after annealing. The AA will lose plasticity when the thermal stress becomes higher than the critical fracture stress.

Thus, the stresses caused by the structural, compositional, or magnetic inhomogeneity, apparently, serve as the key factor for embrittlement of amorphous ribbons after heat treatment. The Fe-based AAs free from Invar effect are structurally more homogeneous and, therefore, more resistant to thermal embrittlement.

We also observed the loss of plasticity in the $Co_{70.5}Fe_{0.5}Cr_4Si_7B_{18}$ and $Fe_{60.8}Co_{20.2}B_{14}Si_5$ AAs (Figure 2).

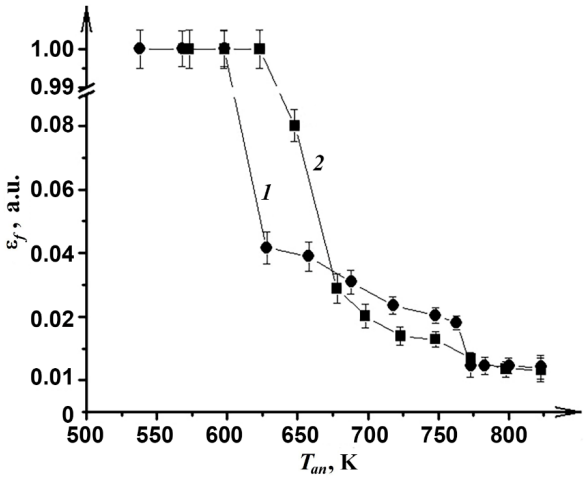


Figure 2. Plasticity behavior of the AAs subjected to heat treatment: *1*, $Co_{70.5}Fe_{0.5}Cr_4Si_7B_{18}$; *2*, $Fe_{60.8}Co_{20.2}B_{14}Si_5$.

It is shown that both AAs pass into a brittle state in two stages. The first abrupt decrease in ε_f (from 1.0 to 0.04–0.08) is observed at temperatures of 625 K and 650 K, respectively, and the second, less abrupt decrease (virtually to zero from 0.04 for the former alloy and from 0.08 for the latter alloy) is stretched over heat treatment intervals of 625–775 K and 650–775 K, respectively. A detailed analysis of the microindent and the plastic deformation zone of numerous diverging "rays" of shear bands (Figure 3) occurring upon indentation allows us to estimate the degree of local plasticity of the AAs.

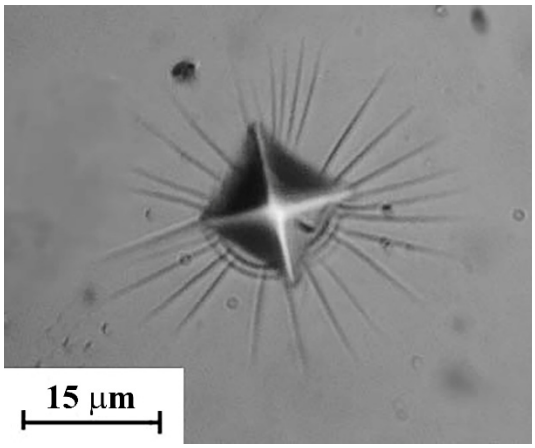


Figure 3. Typical microscopic image of the plastic deformation of AA after indentation with Vickers indenter.

A surface density of plastic deformation zones (ρ) as the number of shear bands reduced to unit area can be used as the criterion for the resulting degree of microdeformation, which changes upon heating. The parameter (ρ) at the specified T_{an} was estimated as $\rho = N_{av}/S$, where N_{av} is the average value of shear bands from 20 indentations at the selected T_{an} and S is the surface area of the AA in the image of each indentation; S = 100 μm × 100 μm = 0.01 mm^2 = const. The photographic enlargement in all images was the same. In addition, the average length (L) of the shear bands formed around the indent can be also used as a parameter of local plasticity (Figure 3). It was interesting to follow the changes in the ρ and L parameters after heat treatment of the AAs and to compare them with the change (drop) in the macroscopic plasticity ε_f at the stage of ductile–brittle transition.

Let us turn to Figure 4, in which the behavior of ρ (Figure 4a) and L of shear bands (Figure 4b) is demonstrated as a function of the annealing temperature by the example of $Fe_{60.8}Co_{20.2}B_{14}Si_5$ AA. It was found that both characteristics noticeably decrease (after annealing at 725 K, by a factor of 5 and 2.5, respectively). In this case, the variation of the plasticity parameters occurs in two stages: After annealing at temperatures below 600 K, both characteristics decrease insignificantly, and the parameter ρ even increases at the early stages of heat treatment (Figure 4a). An abrupt decrease in local plasticity is observed after annealing at temperatures above 600 K.

The decrease in plasticity can certainly be explained by an increase in the parameters of the topological and/or compositional short-range order upon annealing of AAs along with a decrease in the fraction of excess free volume [10,42]. In this case, it should be taken into account that the decrease in plasticity may turn out to be false. Indeed, an increase in the degree of short-range order could lead to a stronger localization of slip and, as a consequence, to a further increase in the shear band power (an average degree of plastic deformation in the shear band as a ratio of the slip step height to the band thickness). However, simple calculations show that an increase in the shear band thickness, which is already very large, is not able to compensate for a substantial decrease in the band density and length in the total degree of deformation realized by the shear bands.

The decrease in the ability to exhibit plastic flow at the microscale (Figure 4) begins at annealing temperatures (near 500 K for the $Fe_{60.8}Co_{20.2}B_{14}Si_5$ AA) that are well below the temperature of macroscopic ductile–brittle transition (T_f ~ 637 K) determined by the macrobending test (Figure 2). The complete disappearance of plastic deformation patterns occurs only as the active crystallization begins at the surface (~750 K) and propagates deep into the samples. Comparison of the graphs in Figures 2 and 4 shows that the actual embrittlement occurs when the decrease in the density and length of shear bands already corresponds to the second stage of abrupt decrease in plasticity. These data fundamentally discord with the conclusions of Kimura and Masumoto [33]. In their opinion, the ability to form shear bands does not undergo any noticeable change (decrease) in the temperature range of the macroscopic ductile–brittle transition. Thus, the phenomenon of embrittlement has two following structural causes, which are apparently related to each other: a decrease in the ability to exhibit plastic flow in amorphous matrix and an abrupt decrease in the resistance to the development of main quasibrittle cracks.

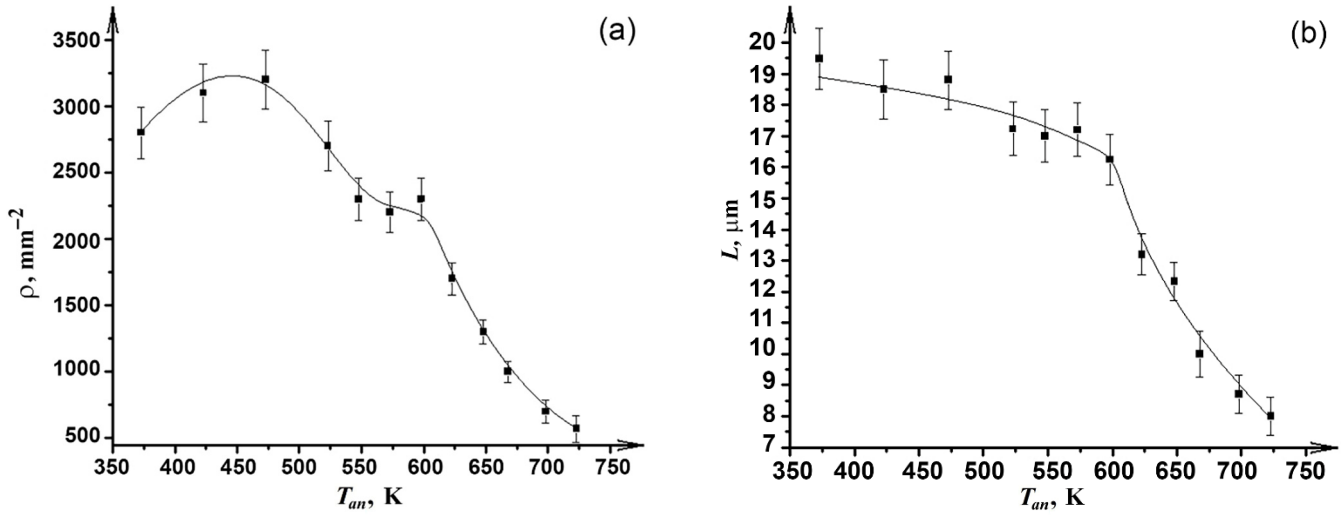


Figure 4. Local plasticity of $Fe_{60.8}Co_{20.2}B_{14}Si_5$ AA as a function of annealing temperature: (**a**) surface density of plastic deformation zones; (**b**) length of shear bands.

3.2. Strengthening Effects upon Crystallization of AAs

The prime causes for the strengthening of AAs upon heat treatment at the initial stages of crystallization ($V_v \leq 0.5$) are as follows:

(1) The difference between Young's moduli of the precipitated crystalline phase and the amorphous matrix, i.e., the "modular" strengthening factor [10]:

$$HV = HV_A\left[1 + V_v\left(\frac{E_A}{E_c}\right)\right], \quad (3)$$

where E_A and E_C are Young's moduli of the amorphous and crystalline phases, respectively; HV_A is the microhardness of the amorphous matrix; and V_v is the volume fraction of crystalline phases.

An example of the implementation of this factor is the $Fe_{70}Cr_{15}B_{15}$ AA, in which the crystallization occurs by eutectic mechanism in a temperature range of 733–783 K [43]. The crystalline eutectic colonies are represented by barrel-shaped globules consisting of alternating nanoplates 44 nm and 28 nm thick, respectively, of Fe_3B iron boride and α(BCC) Fe-Cr solid solution in a ratio of 3:1 (Figure 5).

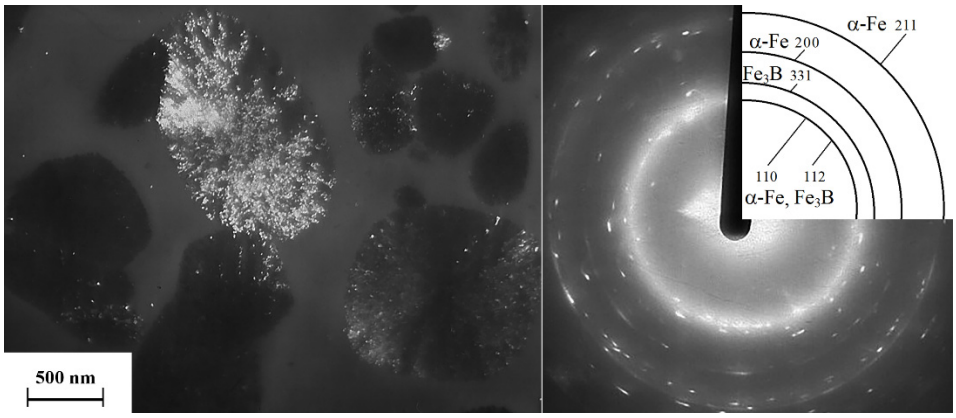


Figure 5. Dark-field image (TEM) of Fe(Cr)-$(Fe,Cr)_3B$ eutectic colonies in amorphous matrix of the $Fe_{70}Cr_{15}B_{15}$ AA annealed at T_{an} = 743 K for 1 h.

Figure 6 shows the linear $HV(V_v)$ dependence calculated on the basis of Equation (3) at the stage of eutectic crystallization of the $Fe_{70}Cr_{15}B_{15}$ AA.

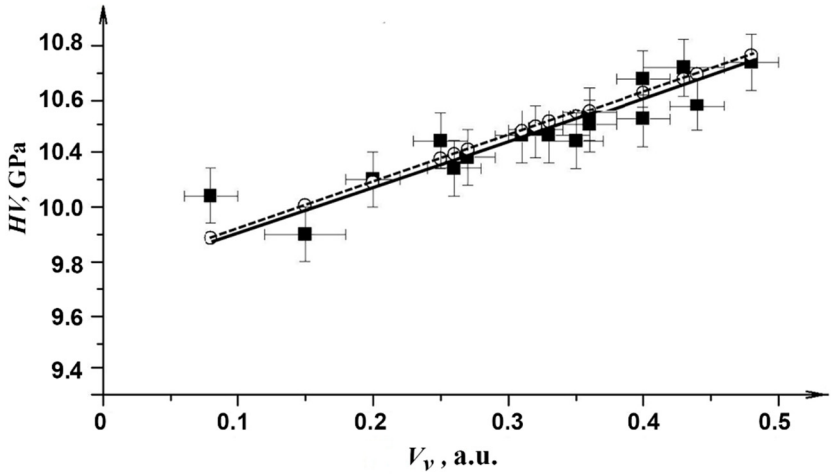


Figure 6. Microhardness as a function of the volume fraction of the crystalline phase for different annealing modes of the $Fe_{70}Cr_{15}B_{15}$ AA: ○—data calculated by Equation (3); ■—experimental data.

As is seen, the experimental points are in satisfactory agreement with the theoretical dependence. This means that, in this case, the main contribution to the strengthening of AAs upon the precipitation of the eutectic phase is due to higher elastic moduli of the crystalline phase particles precipitated in the amorphous matrix.

(2) The interaction of the nanocrystalline phase particles with deformation shear bands propagating in the amorphous matrix, i.e., the "structural" factor of strengthening [10]. An example of the implementation of the structural factor is given by the $Fe_{50}Ni_{33}B_{17}$ AA. With the help of TEM examination results, it was found that, after annealing, the nanocrystalline γ-phase (FCC) particles in the $Fe_{50}Ni_{33}B_{17}$ alloy are of near-equiaxed shape, and their size does not change (≈20 nm) at any temperature–time parameters of heat treatment (T_{an} = 523–723 K, t = 30 min–2 h) (Figure 7) [44]. The stabilization of the nanocrystal size can be explained within the framework of the "crystallization-and-stop" structural model [45]. According to this model, a barrier shell enriched with an alloying element (boron) is formed around γ-Fe-Ni particles, inhibits the growth of nanocrystals, and thus increases the thermal stability of the amorphous matrix [46].

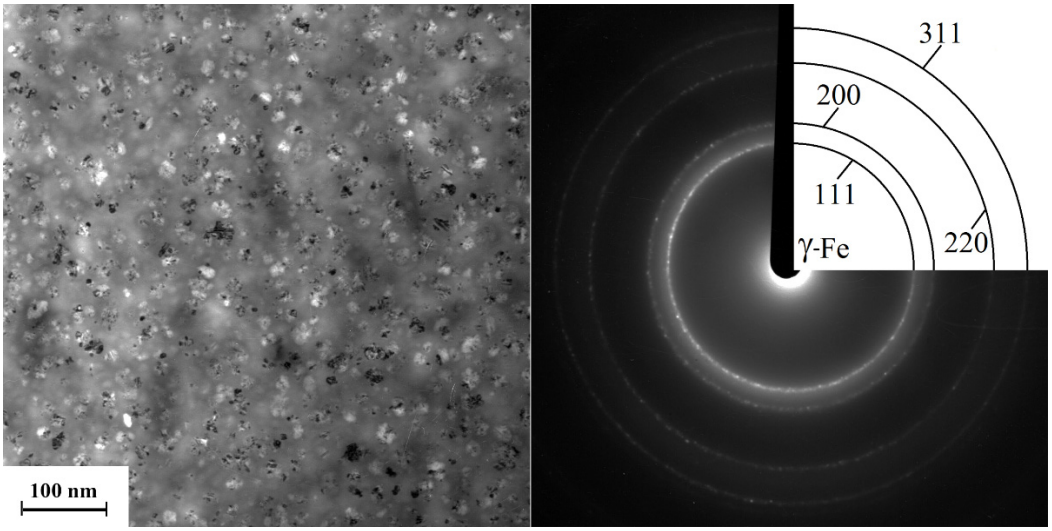


Figure 7. Bright-field image (TEM) of the $Fe_{50}Ni_{33}B_{17}$ AA structure after annealing at T_{an} = 743 K, 1 h.

For this alloy, E_A and E_C are approximately equal. The change in microhardness as a function of the volume fraction (bulk density) of nanoparticles is described by the dependence (K—proportional constant)

$$HV \sim K(V_v)^{1/3} \tag{4}$$

which is close to Orowan's dependence (5) showing the interaction of moving dislocations with incoherent particles of the second phase:

$$\sigma = \sigma_0 + cG\varepsilon\left(\frac{V_v b}{D}\right)^{1/2} \tag{5}$$

where σ is the deforming stress, σ_0 is the deforming stress in a crystal not containing particles, c is a constant equal to 0.1–0.6, G is the shear modulus, V_v is the volume fraction of particles, b is the Burgers vector of gliding dislocations, D is the size of particles, and ε is the degree of plastic deformation.

As seen in Figure 8, there is a noticeable similarity between the effect of the volume fraction of particles (in our case, also the volume density of particles) on strengthening in crystals and in the AAs. The difference lies in the fact that the exponent n is $\frac{1}{2}$ for crystals (Equation (5)), while for AAs it is $^1/_3$ (Equation (4)). This analogy is not unexpected, since the shear bands that implement plastic shear in the amorphous state, in essence, at the mesoscale are effective dislocations, the Burgers vector of which is not determined precisely. In this case, the degree of plastic deformation concentrated in the shear band is hundreds of percent. The lower n indicates that the deceleration of shear bands by particles in AAs is less effective than that in crystals by the Orowan's mechanism.

The interaction of shear bands with nanoparticles in amorphous–nanocrystalline composites obtained upon annealing of iron- and cobalt-based AAs has been studied in detail by TEM. Shear bands were induced by the indentation of the foil edge immediately before TEM examination at a load of 0.01–0.02 N. Then, it was possible to systematize multiple acts of the interaction of shear bands with nanocrystals by the analysis of the electron microscopic images (Table 2) [10,47–49].

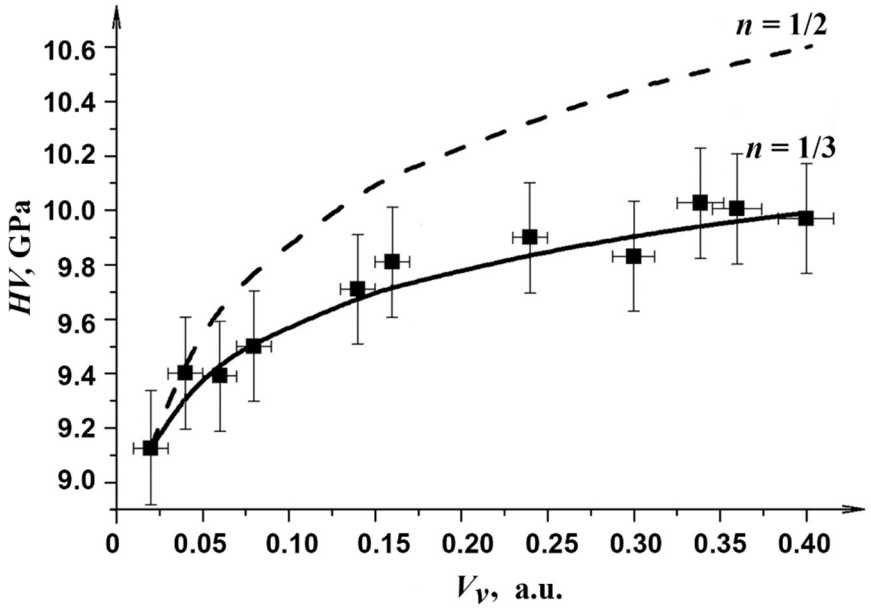


Figure 8. Microhardness as a function of volume fraction of the crystalline phase for all annealing modes of the $Fe_{50}Ni_{33}B_{17}$ AA (solid line) and Orowan's dependence for crystals (dashed line).

Table 2. Classification of mechanisms of interaction between shear bands and nanoparticles in annealed AAs.

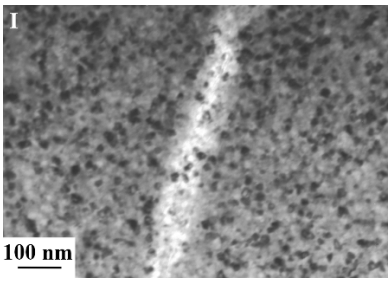
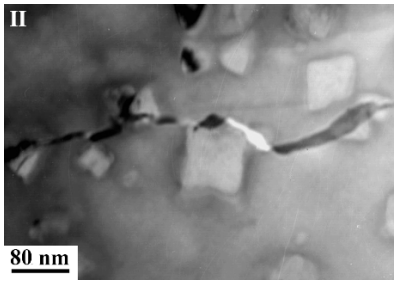
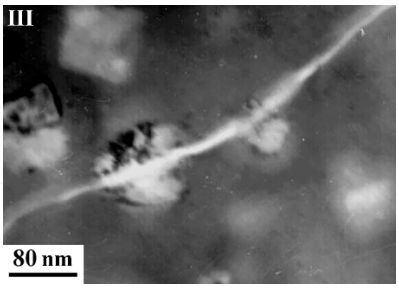
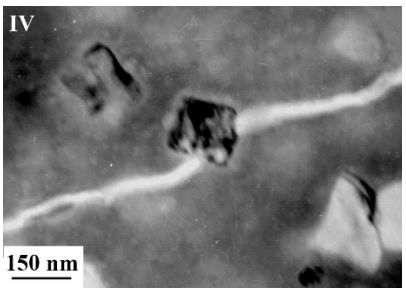
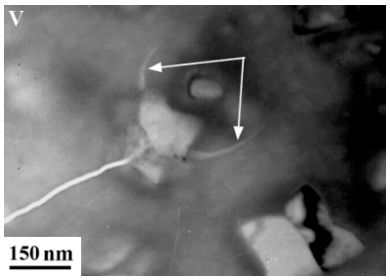
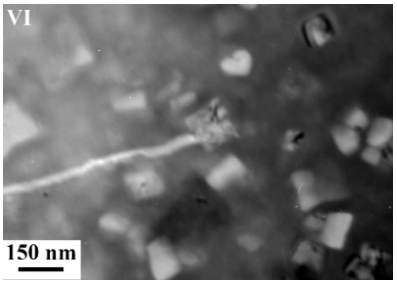
Mechanism	Description	Typical TEM Image
Absorption	The shear band absorbs small nanoparticles without changing the motion trajectory in the amorphous matrix.	
Looping	The shear band bends around the oncoming nanoparticle on its path, changing the motion trajectory in the amorphous matrix. Its motion resembles the process of double transverse slip of a dislocation that overcomes a rigid barrier.	
Cutting	The shear band passes through the nanoparticle, "cutting" it. This case is realized if a shear band propagating in an amorphous matrix can stimulate a dislocation flow in a nanoparticle.	

Table 2. *Cont.*

Mechanism	Description	Typical TEM Image
Accommodation (primary)	A shear band resting on a nanoparticle causes its very large elastic distortions, which, in turn, initiate a shear band in the amorphous matrix on the other side of the nanoparticle. As a rule, the trajectory of movement of the secondary accommodation shear band coincides with the trajectory of the primary shear band.	
Accommodation (secondary)	An elastically stressed nanocrystal initiates several new secondary shear bands from its boundary into an amorphous matrix (indicated by arrows in the photo).	
Braking	The shear band decelerates and stops/becomes stuck at the interface or inside the nanoparticle.	

The main attention in the study of TEM images was given to the morphology of shear bands during their passage through nanoparticles or in close proximity. More than 100 cases of interaction of shear bands with nanoparticles were analyzed. In this case, special attention was paid to the unambiguous identification of shear bands in TEM images.

The section of foil by studied TEM method corresponding to the shear step has a different effective thickness compared to the section of surrounding undeformed matrix. Therefore, the contrast in the TEM image of shear bands is of an absorption nature. In the case when the angle θ between the direction of the incident electron beam and the effective shift realized by the shear band is less than 180°, the shear band is observed as a light band on a dark background. If the angle θ is greater than 180°, then the shear band is observed as a dark band on a light background [50]. Dark-field images obtained in the study of plastically deformed AAs make it possible to reveal a number of morphological features of shear bands: they are "noncrystallographic", i.e., easily change the local plane of their orientation, and are characterized by the presence of branch points. A shear band with a smoothly changing orientation, during passing at some points through a position corresponding to an angle θ equal to 0 or 180°, will be observed on TEM images in the form of a region of light contrast turning into regions of dark contrast, or vice versa.

It was found by the example of the $Fe_{58}Ni_{25}B_{17}$ AA that the determining factor for the change in the mechanism of interaction of shear bands with nanoparticles is the size of nanocrystals (Figure 9) [49].

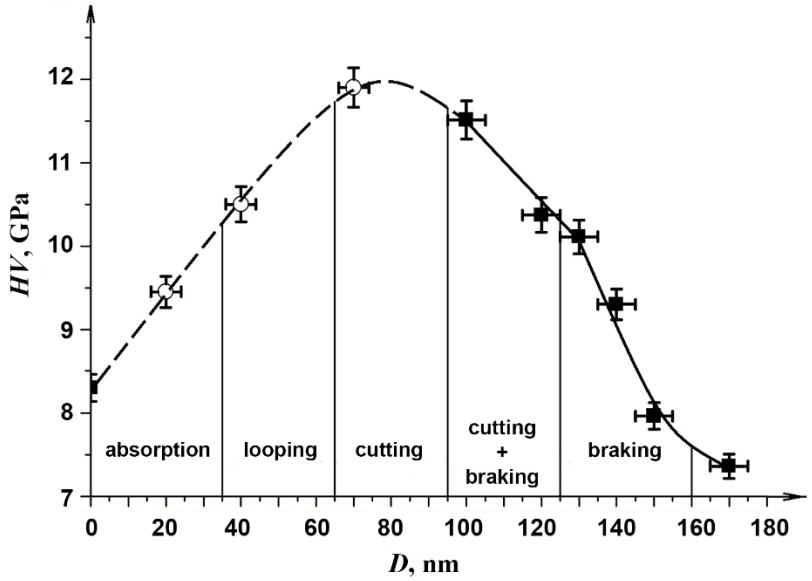


Figure 9. Microhardness of the $Fe_{58}Ni_{25}B_{17}$ AA as a function of the average size of nanoparticles, taking into account the implementation of priority mechanism of interaction between shear bands and nanocrystals.

The $HV = f(D)$ dependence is represented by a curve with maximum. The solid line denotes the microhardness for all realized two-phase states obtained after annealing in the temperature–time ranges of t = 30 min–2 h and T_{an} = 643–673 K, respectively, and the dashed line shows the HV data corresponding to short-term annealing at the earliest stages of nanocrystallization of AAs (t = 3–10 min, T_{an} = 643–673 K).

At D = 80–170 nm, a "normal" $HV = f(D)$ dependence is established, which is similar to the dependence of yield strength (hardness) on grain size for polycrystalline materials, i.e., to the Hall–Petch relationship [51]:

$$\sigma_y(HV) = \sigma_0(HV_0) + kD^{-1/2}, \quad (6)$$

where σ_y is the yield stress; HV is the hardness; σ_0 and HV_0 are the plastic flow stress and hardness in the grain body, i.e., material constants for the starting stress for dislocation movement (or the resistance of the lattice to dislocation motion); k_y is the proportionality coefficient characterizing the "penetrability" of grain boundaries; and D is the average grain size.

In other words, as the nanoparticle size decreases, HV substantially increases. At $D \leq 80$ nm, an "anomalous" dependence $HV = f(D)$ is observed; i.e., a further decrease in D leads to an abrupt decrease in HV. Thus, the mechanisms of "braking" and "cutting" are responsible for the "normal" $HV = f(D)$ relationship, and the mechanisms of "absorption" and "looping" are responsible for the "abnormal" relationship.

3.3. The Phenomenon of Plasticization in AAs

The way to the practical use of amorphous–nanocrystalline composites is obstructed by the problem of low thermal stability as well as by the existence of a very narrow temperature range for the realization of the optimal combination of amorphous and crystalline phases. Up until recently, with regard to the behavior of plasticity of amorphous–nanocrystalline and fully nanocrystalline alloys, there was a general opinion that if high strength could still be obtained, then plasticity at the smallest sizes of nanocrystals or grains was always zero. The problem of the plasticization of AAs and composites on their base has been discussed for a long time [7,9,52]. At present, the evidence demonstrating both good strength and satisfactory ductility for such materials has appeared [10,53–55] as a consequence of more advanced production technologies and the use of additional, sometimes combined, subse-

quent actions on materials. For the first time, the effect of plasticization (some increase in K_{1c} with a significant decrease in HV) was found in the $Co_{70.5}Fe_{0.5}Cr_4Si_7B_{18}$ AA, but more pronounced effects were observed in the $Fe_{53.3}Ni_{26.5}B_{20.2}$ and $Co_{28.2}Fe_{38.9}Cr_{15.4}Si_{0.3}B_{17.2}$ AA (Figure 10a), as well as in $Fe_{58}Ni_{25}B_{17}$ AA (maximum at 653 K) (Figure 10b).

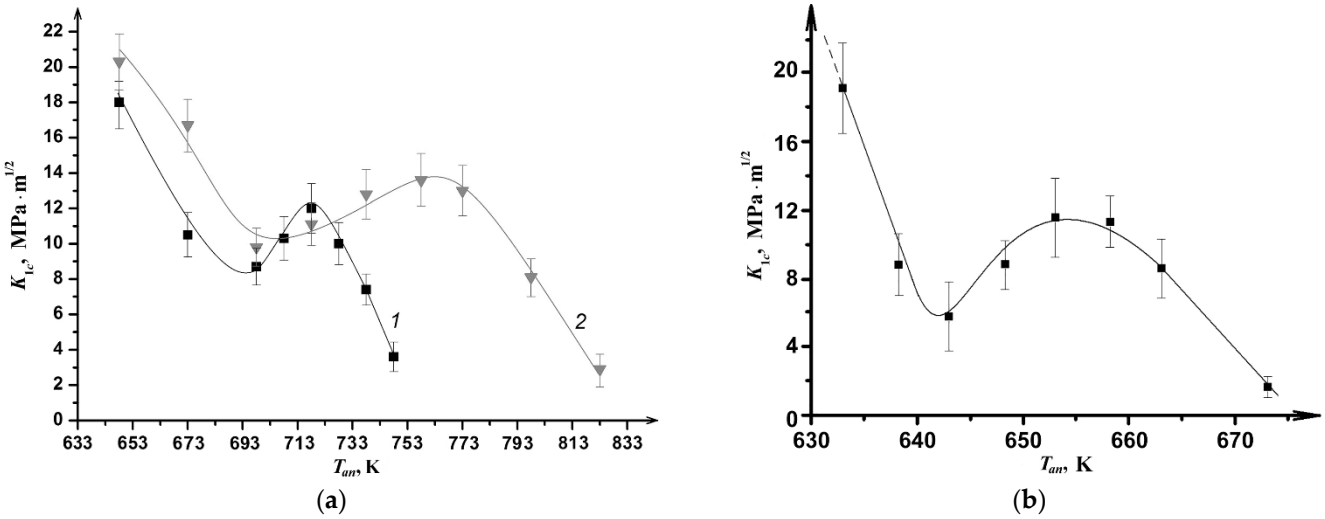


Figure 10. Crack resistance K_{1c} behavior of AAs subjected to annealing: (**a**) $Fe_{53.3}Ni_{26.5}B_{20.2}$ AA (curve *1*) and $Co_{28.2}Fe_{38.9}Cr_{15.4}Si_{0.3}B_{17.2}$ AA (curve *2*); (**b**) $Fe_{58}Ni_{25}B_{17}$ AA.

Let us consider the nature of this phenomenon in detail. Figure 11 shows the graphs of the crack resistance as a function of the structural parameters of the $Fe_{58}Ni_{25}B_{17}$ AA under study. The TEM examination exhibited a noticeable increase in the size and volume density of dispersed α-phase nanoparticles (BCC) in the area of the detected anomaly of mechanical behavior.

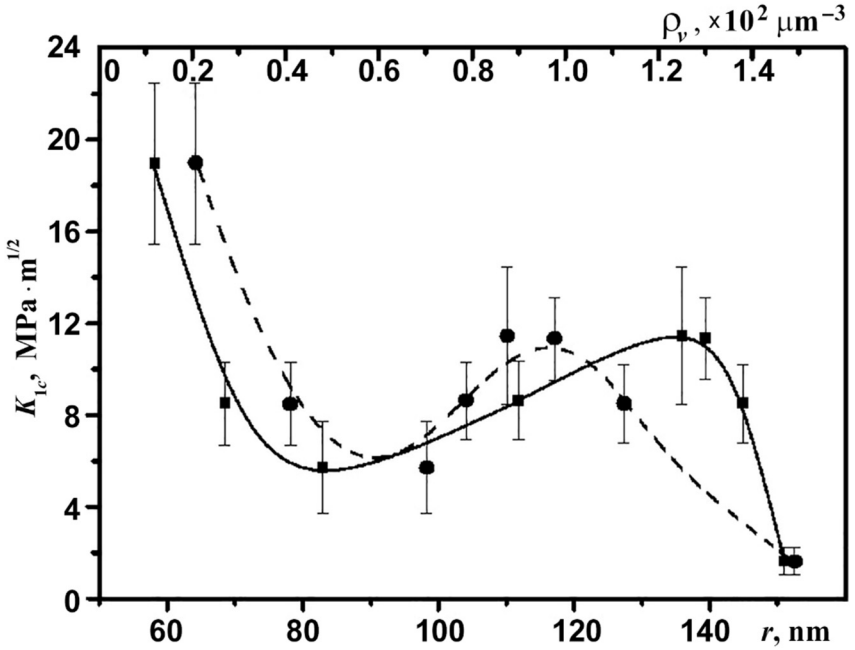


Figure 11. Crack resistance of the $Fe_{58}Ni_{25}B_{17}$ AA as a function of the size of crystalline particles r (dashed line) and their volume density ρ_V (solid line).

The nanocrystals have a clear crystallographic faceting along the $\{100\}_\alpha$-type planes. It is seen that the characteristic particle size, at which the maximum of the K_{1c} parameter is recorded, corresponds to 110–120 nm at a bulk density of 1.3×10^2 μm^{-3} of the crystalline

phase. A further (at higher annealing temperatures) decrease in crack resistance of the alloy is associated with the appearance of $(Fe,Ni)_3B$ borides in the structure and with the complete bulk crystallization of the material (T_{crys} = 723 K).

The phenomenon of plasticization that we discovered is apparently due to the effective arrest of quasibrittle cracks, which arise and grow in the amorphous matrix as a result of the application of an external load. Possible mechanisms of the arrest of propagating cracks in various materials are analyzed in detail in [56]. Unfortunately, the behavior of cracks in amorphous and nanocrystalline alloys was not considered in this book, which, of course, is very interesting. Moreover, the deceleration mechanisms discussed in the monograph cannot be directly used to explain the effect we observed. The theoretical and experimental consideration of the present paper gives grounds to propose a new original mechanism of the deceleration of quasibrittle cracks developing in the amorphous–nanocrystalline state.

Figure 12 shows a typical TEM image of crack behavior in the $Fe_{58}Ni_{25}B_{17}$ AA after controlled annealing at 653 K for 1 h. It is seen that the crack ends in the region of the nanoparticle, which acts as an insurmountable obstacle on the path of crack propagation. Crack arrest begins, presumably, not at the "amorphous matrix–nanocrystal" interface (in this case, both phases have close elastic moduli), but in the vicinity of the nanoparticle upon approaching it. This is due to the fact that an atmosphere of boron atoms, which are present in significant amounts in AAs but are insoluble in the crystalline phase, is formed around the nanoparticles [46]. The Young's modulus of the structure with such atmosphere is substantially higher than that of the amorphous matrix, in which the quasibrittle crack propagates. This should result in a deceleration of the crack or its complete braking. This conclusion is proved, for example, by the fact that the plasticization effect in the $Fe_{58}Ni_{25}B_{17}$ AA with boron is more pronounced than that in the $Co_{70.5}Fe_{0.5}Cr_4Si_7B_{18}$ AA containing silicon, since boron virtually cannot be dissolved in the α-Fe-Ni nanocrystals and, therefore, forms more powerful atmospheres around nanoparticles.

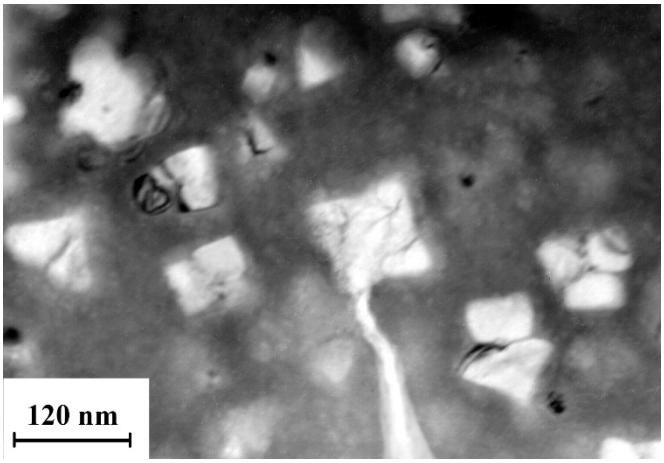


Figure 12. Bright-field image (TEM) of crack arrest on nanocrystalline particle in the $Fe_{58}Ni_{25}B_{17}$ AA annealed at T_{an} = 658 K.

4. Conclusions

(1) The ductile–brittle transition is inherent in all studied compositions of Co- and Fe-based AAs. It is carried out in a rather narrow temperature range: the AA is completely or partially embrittled at a certain annealing temperature T_f ($T_f < T_{crys}$). A feature is that the sharp decrease in ε_f occurs in one stage for some AAs and in two stages for others, depending on the chemical composition, quenching rate, and annealing regime. The ductile–brittle transition is a measure of relaxation processes in AAs and an indicator of their temperature–time stability. Thus, it limits the temperature range of AA heat treatment, which, for example, in the case of soft magnetic materials, should cover the temperature range close to the crystallization temperature.

(2) It has been established that the phenomenon of tempering embrittlement characteristic of the metal–metalloid-type AAs is due to a number of interrelated factors such as a decrease in the susceptibility to plastic flow in amorphous matrix and a sharp decrease in the resistance to the development of main quasibrittle cracks. In addition, stresses caused by the structural, compositional, or magnetic type of inhomogeneity can be an important stimulator of the embrittlement of amorphous ribbons after heat treatment.

(3) The main factors of strengthening upon heat treatment of AAs at the transient stage of their crystallization in the amorphous–nanocrystalline state with the volume fraction of crystals $V_v < 0.5$ are established to be as follows: (a) the "module" factor, i.e., the difference between Young's moduli of the amorphous and nanocrystalline phases, and (b) the "structural" factor, i.e., interaction of shear bands with particles of the nanocrystalline phase precipitating in the amorphous matrix.

(4) The following classification of the mechanisms of the interaction between nanoparticles and shear bands in amorphous–nanocrystalline composites is proposed on the basis of a detailed analysis of electron microscopic images: "absorption", "looping", "cutting", "braking", and primary and secondary "accommodation". It was revealed that the prime cause for the change in mechanisms is the nanoparticle size. However, among the factors that finally determine the nature of the interaction of shear bands and nanoparticles, several should be highlighted: the annealing time, the type of crystal lattice of nanocrystals with which shear bands meet, the speed of shear bands, their mutual orientation with nanoparticles, and the chemical composition of the precipitating phases.

(5) It is shown that the optimal ratio between the amorphous and crystalline phases and their distribution can be achieved after annealing of AAs in the specified temperature–time ranges. In turn, this will provide a unique combination of mechanical properties, i.e., increased strength and, at the same time, a satisfactory ductility of such composite material.

(6) A plasticizing effect (an increase in the crack resistance parameter) was discovered in the temperature range of transition to the amorphous–nanocrystalline state for a number of iron- and cobalt-based AAs. The structural parameters corresponding to this phenomenon have been analyzed. An original mechanism of the arrest of propagating quasibrittle cracks in the zones surrounding the nanoparticles and enriched with metalloid atoms is proposed.

(7) The obtained experimental results contribute to the development of general ideas about the evolution of the structure and mechanical properties of both amorphous and amorphous–nanocrystalline alloys. It was established that AA crystallization has a number of features, and thermal action on a homogeneous amorphous structure can stimulate processes leading to the formation of materials with different structural parameters. Microstructure changes; phase composition; crystallization mechanism; and the size, volume fraction, and morphology of nanocrystals significantly affect the mechanical characteristics of AAs (strength, plasticity, hardness, and crack resistance).

Author Contributions: Conceptualization and methodology, A.G. and I.P.; software, I.P.; validation, A.G. and I.P.; formal analysis, I.P.; investigation, A.G. and I.P.; resources, A.G.; data curation, I.P.; writing—original draft preparation, I.P.; writing—review and editing, A.G. and I.P.; visualization, I.P.; supervision and project administration, A.G.; funding acquisition, I.P. All authors have read and agreed to the published version of the manuscript.

Funding: The reported study was funded by RFBR, project number 20-08-00341.

Institutional Review Board Statement: Not applicable.

Informed Consent Statement: Not applicable.

Data Availability Statement: Not applicable.

Acknowledgments: The authors are grateful to their colleague Nadezhda Shurygina for long-term fruitful cooperation.

Conflicts of Interest: The authors declare no conflict of interest. The funders had no role in the design of the study; in the collection, analyses, or interpretation of data; in the writing of the manuscript; or in the decision to publish the results.

References

1. Greer, A.L. Metallic Glasses. In *Physical Metallurgy*, 5th ed.; Laughlin, D.E., Hono, K., Eds.; Elsevier: Amsterdam, The Netherlands, 2014; Volume 1, pp. 305–385; ISBN 978-0-444-53770-6.
2. Ashby, M.F.; Greer, A.L. Metallic glasses as structural materials. *Scr. Mater.* **2006**, *54*, 321–326. [CrossRef]
3. Khonik, V.; Kobelev, N. Metallic Glasses: A New Approach to the Understanding of the Defect Structure and Physical Properties. *Metals* **2019**, *9*, 605. [CrossRef]
4. Egami, T.; Iwashita, T.; Dmowski, W. Mechanical properties of metallic glasses. *Metals* **2013**, *3*, 77–113. [CrossRef]
5. Glezer, A.M.; Potekaev, A.I.; Cheretaeva, A.O. *Thermal and Time Stability of Amorphous Alloys*; CRC Press: Boca Raton, FL, USA, 2017; ISBN 978-1-1380-6827-8.
6. Trexler, M.M.; Thadhani, N.N. Mechanical properties of bulk metallic glasses. *Prog. Mater. Sci.* **2010**, *55*, 759–839. [CrossRef]
7. Schuh, C.A.; Hufnagel, T.C.; Ramamurty, U. Mechanical behavior of amorphous alloys. *Acta Mater.* **2007**, *55*, 4067–4109. [CrossRef]
8. Inoue, A.; Hashimoto, K. (Eds.) *Amorphous and Nanocrystalline Materials: Preparation, Properties, and Applications*; Springer: Berlin/Heidelberg, Germany, 2001; ISBN 978-3-540-67271-5.
9. Li, F.C.; Liu, T.; Zhang, J.Y.; Shuang, S.; Wang, Q.; Wang, A.D.; Wang, J.G.; Yang, Y. Amorphous-nanocrystalline alloys: Fabrication, properties, and applications. *Mater. Today Adv.* **2019**, *4*, 100027. [CrossRef]
10. Glezer, A.M.; Permyakova, I.E. *Melt-Quenched Nanocrystals*; CRC Press: Boca Raton, FL, USA, 2013; ISBN 978-1-4665-9414-2.
11. Permyakova, I.; Glezer, A. Amorphous-Nanocrystalline Composites Prepared by High-Pressure Torsion. *Metals* **2020**, *10*, 511. [CrossRef]
12. Aronin, A.; Abrosimova, G. Specific Features of Structure Transformation and Properties of Amorphous-Nanocrystalline Alloys. *Metals* **2020**, *10*, 358. [CrossRef]
13. Louzguine-Luzgin, D.V.; Louzguina-Luzgina, L.V.; Churyumov, A.Y. Mechanical properties and deformation behavior of bulk metallic glasses. *Metals* **2013**, *3*, 1. [CrossRef]
14. Greer, A.L.; Cheng, Y.Q.; Ma, E. Shear bands in metallic glasses. *Mater. Sci. Eng. R Rep.* **2013**, *74*, 71–132. [CrossRef]
15. Spaepen, F. A microscopic mechanism for steady state inhomogeneous flow in metallic glasses. *Acta Metall.* **1977**, *25*, 407–415. [CrossRef]
16. Abrosimova, G.E.; Aronin, A.S.; Zver'kova, I.I.; Kir'yanov, Y.V. Phase Transformations upon Crystallization of Amorphous Al-Ni-Re Alloys. *Phys. Met. Metallogr.* **2002**, *94*, 102–107.
17. Louzguine, D.V.; Inoue, A. Nanoparticles with icosahedral symmetry in Cu-based bulk glass former induced by Pd addition. *Scr. Mater.* **2003**, *48*, 325–1329. [CrossRef]
18. Fan, C.; Inoue, A. Ductility of bulk nanocrystalline composites and metallic glasses at room temperature. *Appl. Phys. Lett.* **2000**, *77*, 46–48. [CrossRef]
19. Qiao, J.; Jia, H.; Liaw, P.K. Metallic glass matrix composites. *Mater. Sci. Eng. R Rep.* **2016**, *100*, 1–69. [CrossRef]
20. Shi, Y.F.; Falk, M.L. A computational analysis of the deformation mechanisms of a nanocrystal-metallic glass composite. *Acta Mater.* **2008**, *56*, 995–1000. [CrossRef]
21. Hajlaoui, K.; Yavari, A.R.; Doisneau, B.; LeMoulec, A.; Botta, W.J.F.; Vaughan, G.; Greer, A.L.; Inoue, A.; Zhang, W.; Kvick, A. Shear delocalization and crack blunting of a metallic glass containing nanoparticles: In situ deformation in TEM analysis. *Scr. Mater.* **2006**, *54*, 1829–1834. [CrossRef]
22. Luborsky, F.E.; Walter, J.L. Stability of amorphous metallic alloys. *J. Appl. Phys.* **1976**, *47*, 3648–3650. [CrossRef]
23. Glezer, A.M.; Molotilov, B.V.; Utevskaya, O.L. Structural reasons of temper brittleness of amorphous metal-metalloid alloys. *Phys. Met. Metallogr.* **1984**, *58*, 991–1000. (In Russian)
24. Kimura, H.; Ast, D.G. Structural relaxation and embrittlement of amorphous $Fe_{40}Ni_{40}P_{14}B_6$. In Proceedings of the 4th International Conference on Rapidly Quenched Metals, Sendai, Japan, 24–28 August 1981; Masumoto, T., Suzuki, K., Eds.; Japan Institute of Metals: Sendai, Japan, 1982; Volume 1, pp. 475–478.
25. Glezer, A.M.; Permyakova, I.E. Modern ideas about methods for studying the mechanical properties of metallic glasses (review). *Deform. Fract. Mater.* **2006**, *3*, 2–11. (In Russian)
26. Novikov, N.V.; Dub, S.N.; Bulychov, S.I. Methods of microtesting for crack resistance. *Ind. Lab. Diagn. Mater.* **1988**, *54*, 60–67. (In Russian)
27. Feodorov, V.A.; Permyakova, I.E.; Kapustin, A.N. Microindentation as a perspective method for determination of mechanical properties of ribbon metallic glasses. *J. Guangdong Non-Ferr. Met.* **2005**, *15*, 185–187.
28. Evans, A.G.; Charles, E.A. Fracture Toughness Determinations by Indentation. *J. Am. Ceram. Soc.* **1976**, *59*, 371–372. [CrossRef]
29. Glezer, A.M.; Permyakova, I.E.; Fedorov, V.A. Crack resistance and plasticity of amorphous alloys under microindentation. *Bull. Russ. Acad. Sci. Phys.* **2006**, *70*, 1599–1603.

30. Scott, M.G. Thermal stability and crystallization of metallic glasses. *Met. Technol.* **1980**, *7*, 133–141. [CrossRef]
31. Latuskiewicz, J.; Zielinaki, P.; Matyja, M. Role of iron and silicon in embrittlement of metallic glasses. In Proceedings of the 4th International Conference on Rapidly Quenched Metals, Sendai, Japan, 24–28 August 1981; Masumoto, T., Suzuki, K., Eds.; Japan Institute of Metals: Sendai, Japan, 1982; Volume 2, pp. 1381–1384.
32. Glezer, A.M.; Blinova, E.N.; Permyakova, I.E.; Cheretaeva, A.O. The ductile-to-brittle transition and the temperature and temporal stability of amorphous alloys. *Bull. Russ. Acad. Sci. Phys.* **2015**, *79*, 1141–1145. [CrossRef]
33. Kimura, H.; Masumoto, T. Strength, ductility and toughness—A study in model mechanics. In *Amorphous Metallic Alloys*; Luborsky, F.E., Ed.; Butterworth & Co., Ltd.: London, UK, 1983; pp. 187–230; ISBN 978-0-408-11030-3.
34. Zhang, H.-Y.; Zhang, Z.-Y.; Xu, Y.-F.; Xia, A.-L.; Li, W.-H.; Wang, F.-C.; Chen, S.-S.; Sisó, G. Microstructure and magnetocaloric properties of partially crystallized $Gd_{60}Co_{30}Fe_{10}$ amorphous alloy prepared by different solidification cooling rates. *Rare Met.* **2021**, *41*, 246–253. [CrossRef]
35. Yavari, A.R. Absence of Thermal Embrittlement in some Fe-B and Fe-Si-B Glassy Alloys. *Mater. Sci. Eng.* **1988**, *98*, 491–493. [CrossRef]
36. Chi, G.C.; Chen, H.S.; Miller, C.E. The influence of quenching procedures on the kinetics of embrittlement in a $Fe_{40}Ni_{40}B_{20}$ metallic glass. *J. Appl. Phys.* **1978**, *49*, 1715–1717. [CrossRef]
37. Allia, P.; Tiberto, P.; Baricco, M.; Vinai, F. Improved ductility of nanocrystalline $Fe_{73.5}Nb_3Cu_1Si_{13.5}B_9$ obtained by direct-current joule heating. *Appl. Phys. Lett.* **1993**, *63*, 2759–2761. [CrossRef]
38. Hagiwara, M.; Inoue, A.; Masumoto, T. The critical thickness for the formation of Ni-Si-B amorphous alloys. *Metall. Trans. A* **1981**, *12*, 1027–1031. [CrossRef]
39. Takahashi, M.; Koshimura, M.; Abuzuka, T. Phase Diagram of Amorphous and Crystallized Fe-B Alloy System. *Jpn. J. Appl. Phys.* **1981**, *20*, 1821–1832. [CrossRef]
40. Ok, H.N.; Morrish, A.H. Mössbauer study of amorphous $Fe_{82}B_{12}Si_6$. *Phys. Rev. B* **1980**, *22*, 4215–4222. [CrossRef]
41. Ohkubo, T.; Kai, H.; Hirotsu, Y. Structural modeling of Pd-Si and Fe-Zr-B amorphous alloys based on the microphase separation model. *Mater. Sci. Eng. A* **2001**, *304-306*, 300–304. [CrossRef]
42. Betekhtin, V.I.; Kadomtsev, A.G.; Kipyatkova, A.Y.; Glezer, A.M. Excess free volume and mechanical properties of amorphous alloys. *Phys. Solid State* **1998**, *40*, 74–78. [CrossRef]
43. Glezer, A.M.; Permyakova, I.E.; Shurygina, N.A.; Rassadina, T.V. Structural features of crystallization and hardening of amorphous alloy in the Fe-Cr-B system. *Inorg. Mater. Appl. Res.* **2012**, *3*, 23–27. [CrossRef]
44. Glezer, A.M.; Manaenkov, S.E.; Permyakova, I.E.; Shurygina, N.A. Effect of nanocrystallization on the mechanical behavior of Fe-Ni-based amorphous alloys. *Russ. Metall. (Met.)* **2011**, *2011*, 947–955. [CrossRef]
45. Chin, T.-S.; Lin, C.Y.; Lee, M.C.; Huang, R.T.; Huang, S.M. Bulk nanocrystalline alloys. *Mater. Today* **2009**, *12*, 34–39. [CrossRef]
46. Glezer, A.M.; Gorshenkov, M.V.; Zhukov, D.G.; Korchuganova, O.A.; Aleev, A.A.; Boll, T.; Shurygina, N.A.; Shchetinin, I.V. Pinning of nanocrystals growth at Fe-Ni-B amorphous alloy crystallization: Atom probe investigations. *Mater. Lett.* **2015**, *160*, 339–342. [CrossRef]
47. Glezer, A.M.; Manaenkov, S.E.; Permyakova, I.E. Structural mechanisms of plastic deformation of amorphous alloys containing crystalline nanoparticles. *Bull. Russ. Acad. Sci. Phys.* **2007**, *71*, 1702–1707. [CrossRef]
48. Glezer, A.M.; Permyakova, I.E.; Manaenkov, S.E. The mechanisms of interaction of slip bands with nanoparticles in amorphous-crystalline alloys. *Bull. Russ. Acad. Sci. Phys.* **2008**, *72*, 1265–1266. [CrossRef]
49. Glezer, A.M.; Shurygina, N.A.; Zaichenko, S.G.; Permyakova, I.E. Interaction of deformation shear bands with nanoparticles in amorphous-nanocrystalline alloys. *Russ. Metall. (Met.)* **2013**, *2013*, 235–244. [CrossRef]
50. Glezer, A.M.; Molotilov, B.V. *Structure and Mechanical Properties of Amorphous Alloys*; Metallurgy: Moscow, Russia, 1992; pp. 1–208; ISBN 5-299-00907-1. (In Russian)
51. Shtremel, M.A. *The Strength of Alloys*; NUST MISiS: Moscow, Russia, 1997; Volume 2, pp. 1–526. ISBN 5-87623-015-4. (In Russian)
52. Inoue, A. Stabilization of metallic supercooled liquid and bulk amorphous alloys. *Acta Mater.* **2000**, *48*, 279–306. [CrossRef]
53. Glezer, A.M.; Permyakova, I.E.; Manaenkov, S.E. Plasticizing effect in the transition from an amorphous state to a nanocrystalline state. *Dokl. Phys.* **2008**, *53*, 8–10. [CrossRef]
54. Hays, C.C.; Kim, C.P.; Johnson, W.L. Microstructure Controlled Shear Band Pattern Formation and Enhanced Plasticity of Bulk Metallic Glasses Containing in situ Formed Ductile Phase Dendrite Dispersions. *Phys. Rev. Lett.* **2000**, *84*, 2901–2904. [CrossRef]
55. Qiao, J. In-situ Dendrite / Metallic Glass Matrix Composites: A Review. *J. Mater. Sci. Technol.* **2013**, *29*, 685–701. [CrossRef]
56. Finkel, V.M. *Physical Principles of Fracture Deceleration*; Metallurgy: Moscow, Russia, 1977. (In Russian)